Electronic Supplementary Information

Electron-Rich Pyrimidine Rings Enabling Crystalline Carbon Nitride for High-Efficiency Photocatalytic Hydrogen Evolution Coupled with Benzyl Alcohol Selective Oxidation

Zhi Lin, [a] Yiqing Wang, [a] Ta Thi Thuy Nga, [b] Jie Zhang, [c] Ruizhe Wang, [a] Zhengqi Zhang, [a] Yufei Xu, [a] Daming Zhao, [d] Chung-Li Dong [b] and Shaohua Shen* [a]

a. International Research Center for Renewable Energy, State Key Laboratory of Multiphase Flow in Power Engineering, Xi'an Jiaotong University, Shaanxi, 710049, China.
E-mail: shshen_xjtu@mail.xjtu.edu.cn
b. Department of Physics, Tamkang University, New Taipei City, 25137, Taiwan
c. School of Civil and Architecture Engineering, Xi'an Technological University, Xi'an 710021, China
d. School of Advanced Energy, Sun Yat-sen University, Shenzhen 518107, China

Content

1. Experimental section

1.1. Materials

Melamine ($C_3H_6N_6$, ≥99.0%), cyanuric acid ($C_3H_3N_3O_3$, ≥99.0%), 2,4,6-triamine-pyrimidine (TAP, ≥99.0%), potassium chloride (KCl, ≥99.0%), lithium chloride (LiCl, ≥99.0%), dimethyl sulfoxide (DMSO, AR) and benzyl alcohol (C_7H_8O, AR) were purchased from Sinopharm Chemical Reagent Corp., P. R. China. All the materials were of analytical purity and used without further purification.

1.2. Catalysts preparation

High crystalline carbon nitride (CCN-Pr$_x$) samples containing pyrimidine rings were synthesized via a two-step self-assembly and molten-salt annealing strategy. Firstly, x mg of TAP (x = 0, 20, 40, 60, 80) and (500-x) mg of melamine were dissolved in 20 mL DMSO to obtain solution A, and then cyanuric acid (510 mg) was dissolved in 10 mL DMSO to obtain solution B. Subsequently, solution B was added dropwise into solution A under magnetic stirring, and the supramolecular precursor precipitate (MCA-x) was collected after washing and drying. After that, the MCA-x was ground with KCl (2.2 g) and LiCl (1.8 g) in the glovebox, and then the mixture was annealed at 550 °C for 4 h under Ar atmosphere. Finally, the solid was washed with boiling deionized water several times and dried under vacuum at 60 °C for 12 h to obtain CCN-Pr$_x$, where x represents the feeding amounts (mg) of TAP in precursors. As reference, the amorphous PCN was prepared by calcining MCA-0 at 550 °C for 4 h and named CN.

1.3. Characterizations

Powder X-ray diffraction (XRD) patterns were recorded on a diffractometer (X'pert Pro MPD, PANalytical) with Cu Kα irradiation (wavelength = 1.5406 Å). Fourier transforms infrared (FT-IR) spectra were recorded on a spectrometer (Vertex 70, Bruker) using the KBr pellet technique. The transmission electron microscopy

(TEM) images were obtained by a transmission electron microscope (Tecnai G2 F30, FEI). Scanning electron microscopy (SEM) images were obtained by a field-emission scanning electron microscope (JSM-7800F, JEOL). X-ray photoelectron spectroscopy (XPS) was carried out on a spectrometer (Axis-Ultra DLD, Kratos) with a monochromatized Al Kα line source (1486.6 eV), and all the binding energies were calibrated by referencing C 1s to 284.8 eV. Ultraviolet-visible-near infrared diffuse reflectance spectra (UV-vis-NIR DRS) were recorded on a UV-vis-NIR spectrophotometer (Cary5000, Agilent) in the range of 300-800 nm. The steady-state photoluminescence (PL) emission spectra and time-resolved PL (TRPL) spectra were obtained on a fluorescent spectrophotometer (QM-4, PTI) at an excitation wavelength of 420 nm. Surface photovoltage (SPV) spectra were measured at room temperature using a self-made measurement system, equipped with a grating monochromator (Omni-λ3007, Zolix), a 500 W Xe lamp (CHF-XM500, PerfectLight), a lock-in amplifier (SR830-DSP) with an optical chopper (SR540) and a photovoltaic cell. Surface area measurements were carried out by nitrogen adsorption (ASAP 2020 plus, Micromeritics) using the Brunauer-Emmette-Teller (BET) method. Electron paramagnetic resonance (EPR) experiments were performed on an X-band spectrometer (EMX, Bruker) and microwave frequency at 9.40 GHz.

1.4. Photocatalytic measurements

The photocatalytic performances of resultant samples for H_2 evolution with the selective oxidation of benzyl alcohol were implemented in a hermetic Pyrex glass reactor (105 mL), and a 300 W Xe lamp (Microsolar 300, Beijing Perfectlight) equipped with an AM1.5G filter was used as the light source. In a typical reaction, 20 mg of photocatalyst powders were dispersed into the H_2O (79 mL) and benzyl alcohol (1 mL) solution. 2.0 wt% Pt cocatalyst was in-situ loaded on the photocatalyst by photodeposition of H_2PtCl_6. The reactor was purged with argon for 30 min before reaction to remove residual air, and the reaction temperature was controlled at 35 ºC by a cooling water flow during the whole experiment. The evolved gas was quantitatively

determined using a gas chromatograph (5Å molecular sieve column, argon as the carrier gas) equipped with a thermal conductivity detector (TCD), and the liquid product was characterized by high-performance liquid chromatography (HPLC).

The measurement of apparent quantum yield (AQY) for hydrogen evolution was carried out under the same photocatalytic reaction condition with different band-pass filters (365, 380, 400, 420, 450, 500, 550 and 600 nm). The number of incident photons was determined from a spectroradiometer (AvaSpec-2048-USB2, Netherlands). The AQY value was obtained according to the following equation (1).

$$\mathrm{AQY}(\%) = \frac{\text{Number of reacted electrons}}{\text{Number of incident photons}} \times 100\% = \frac{\text{Number of evolved } H_2 \text{ molecules} \times 2}{\text{Number of incident photons}} \times 100\% \quad (1)$$

The solar-to-hydrogen efficiency (STH) was evaluated using a 300 W Xe lamp (Microsolar 300, Beijing Perfectlight) equipped with an AM1.5G filter (100 mW cm^{-2}) as the simulated solar light source, and the irradiated area was set to 2.25 cm^2. STH was calculated according to equation (2).

$$\mathrm{STH}(\%) = \frac{Energy\ of\ generated\ hydrogen}{Solar\ energy\ irradiating\ the\ reactor} \times 100\% \quad (2)$$

The benzyl alcohol conversion and benzaldehyde selectivity were calculated according to equations (3) and (4). The BA and BD respectively represent benzyl alcohol and benzaldehyde.

$$\mathrm{Conversion}(\%) = \frac{n_{initial\ BA} - n_{residual\ BA}}{n_{initial\ BA}} \times 100\% \quad (3)$$

$$\mathrm{Selectivity}(\%) = \frac{n_{produced\ BD}}{n_{initial\ BA} - n_{residual\ BA}} \times 100\% \quad (4)$$

1.5. Mott–Schottky experiments

Mott–Schottky experiments were carried out on an electrochemical workstation (CHI 760D, CH Instrument) using a three-electrode cell system, with platinum foil and Ag/AgCl used as the counter and reference electrodes, respectively. A Na_2SO_4 aqueous solution (0.5 M) was used as the electrolyte. To prepare the working electrodes, 1 mg of powder was dispersed into 1 mL ethanol/H_2O solution (0.5 mL/0.5 mL) to get a turbid liquid, and 10 μL of Nafion 117 solution (5 wt.%) was added as a binder. With the formed suspension (3 μL) dropped on a polished glassy carbon electrode, the working electrode was obtained after completely dried.

1.6. Computational Details

First-principles density functional theory (DFT) calculations were performed using the CASTEP code.[1] The generalized gradient approximation (GGA) of Perdew-Burke-Ernzerhof (PBE) was employed for the electronic exchange and correlation. The kinetic energy cut-off was chosen to be 450 eV. Brillouin zone integration was sampled with 3×3×1 and 3×3×1 Monkhorst-Pack mesh K-points for calculation. The slabs were set by a vacuum region of 20 Å. The self-consistent total energy convergence criteria are less than 10^{-5} eV per atom, and the positions of atoms were optimized until Hellman–Feynman force on each atom was smaller than 0.01 eV $Å^{-1}$.

2. Supporting Data

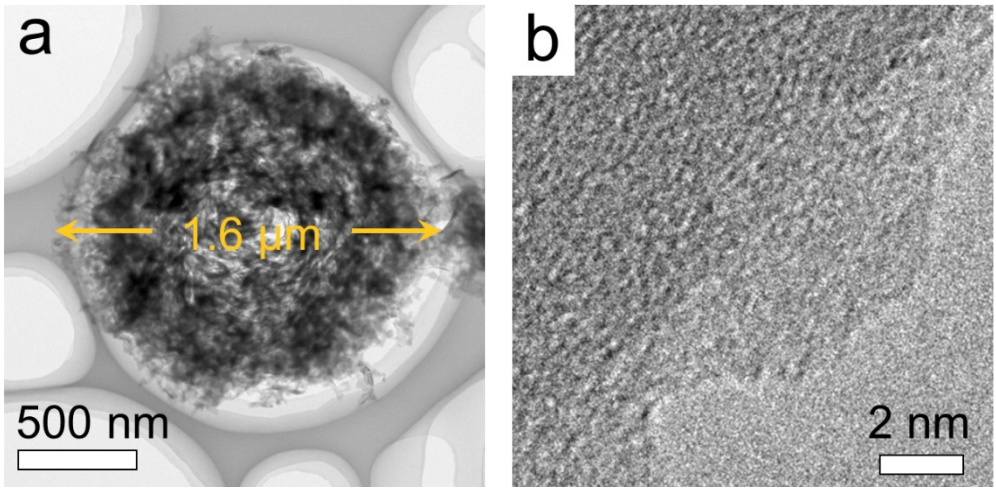

Fig. S1 a) TEM and b) HRTEM images of CN.

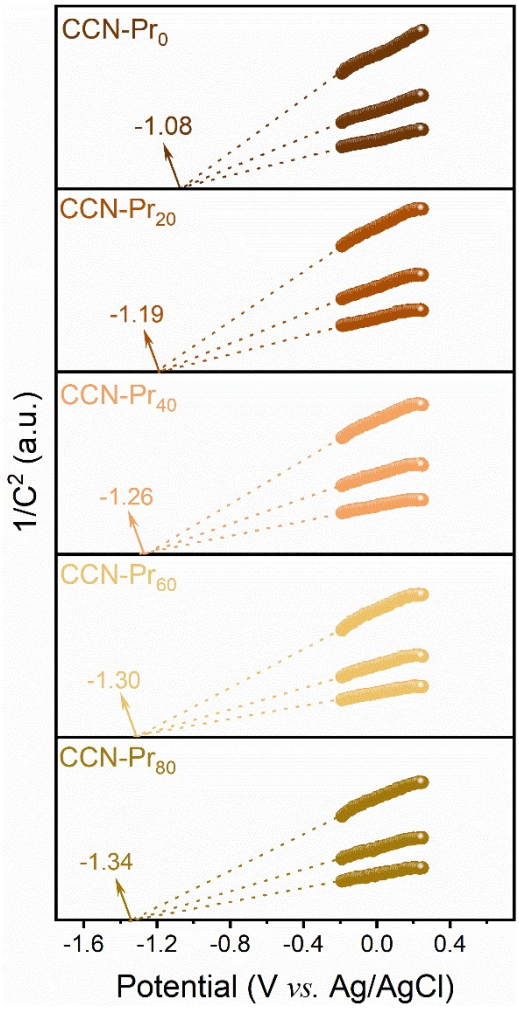

Fig. S2 Mott-Schottky plots of CCN-Pr$_x$ (Potentials *vs*. Ag/AgCl).

Mott-Schottky plots were used to determine the flatband potentials thus to further estimate the conduction band (CB) positions of as-prepared CCN-Pr$_x$ samples. The Mott-Schottky method is based on the Mott-Schottky relation,[2] which was shown in equation (5):

$$\frac{1}{C^2} = \frac{2}{e\epsilon\epsilon_0 N_d A^2}\left(V - V_{fb} - \frac{K_B T}{e}\right) \quad (5)$$

in which C, e, N_d, A, V, V_{fb}, K_B, and T represents the interfacial capacitance, electron charge, electron donor density, exposed area of the electrode, applied potential,

flatband potential, Boltzmann constant, and absolute room temperature, respectively. Given the typical n-type characteristics of all CCN-Pr_x samples as indicated by the positive slope of the plot (Fig. S2), the V_{fb} values could be determined from the intercept between x-axis and the extrapolation of the straight tangent line of the plot of $1/C^2$ as a function of V, to be -1.08, -1.19, -1.26, -1.30, and -1.34 V (*vs*. Ag/AgCl) for CCN-Pr_0, CCN-Pr_{20}, CCN-Pr_{40}, CCN-Pr_{60}, and CCN-Pr_{80}, respectively. Based on the Nernst equation, the V_{fb} values of CCN-Pr_0, CCN-Pr_{20}, CCN-Pr_{40}, CCN-Pr_{60}, and CCN-Pr_{80} could be determined as -0.47, -0.58, -0.65, -0.69, and -0.73 V (*vs*. RHE), respectively (Fig. 3c). According to previous reports, PCN, as a typical n-type semiconductor, the true CB potential is very close to its flatband potential, thus the flatband potential can be used instead of the estimated CB potential.[3,4]

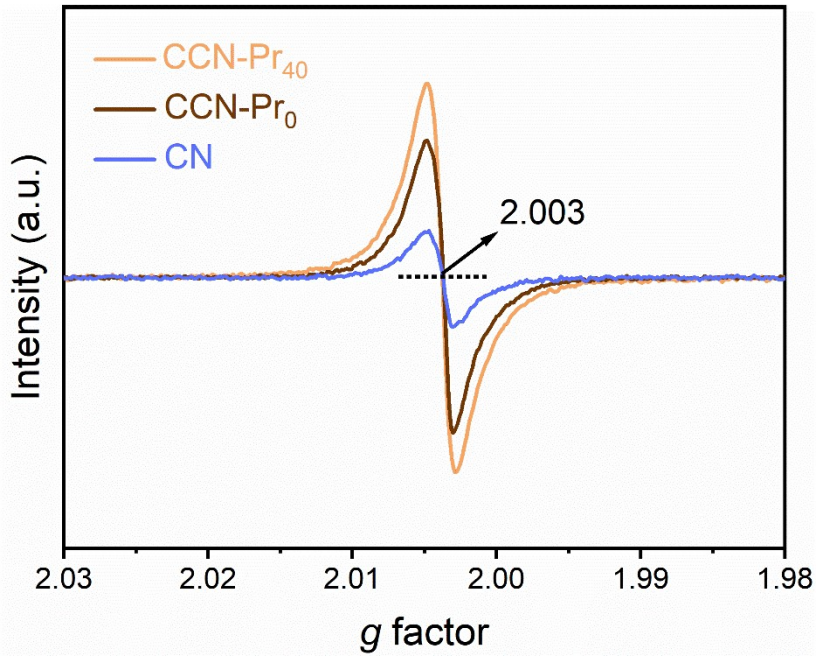

Fig. S3 EPR spectra of CN, CCN-Pr_0, and CCN-Pr_{40}.

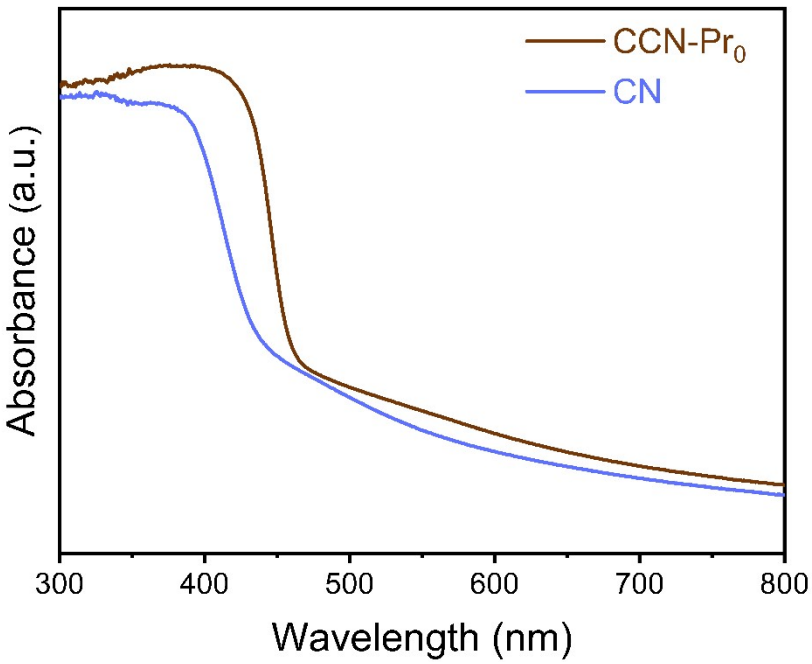

Fig. S4 Ultraviolet-visible diffuse reflectance spectra of CN and CCN-Pr_0.

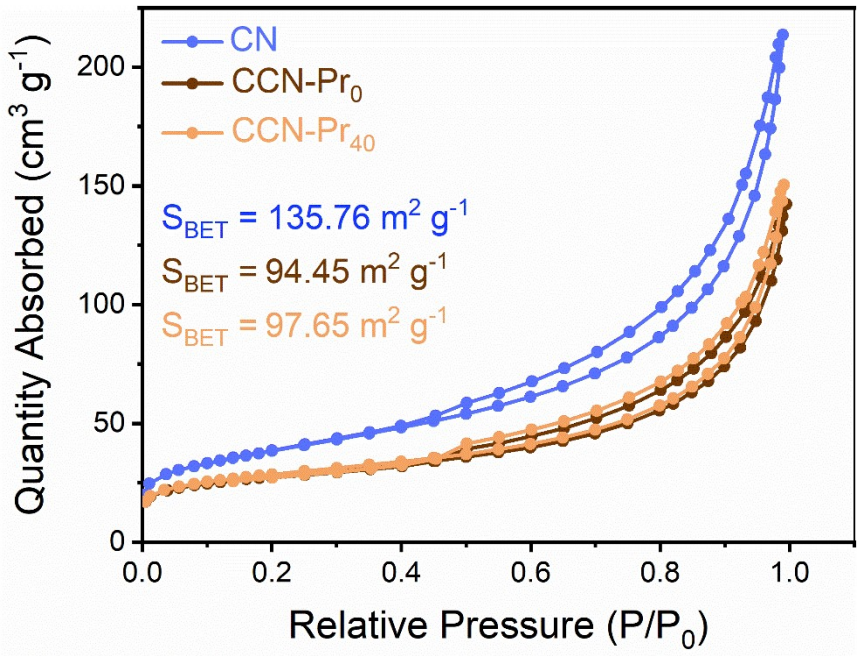

Fig. S5 Nitrogen adsorption-desorption isotherms for CN, CCN-Pr_0, and CCN-Pr_{40}.

As revealed in nitrogen adsorption-desorption isotherms, the specific surface area is observed to be very close for CCN-Pr_0 (94.45 m^2/g) and CCN-Pr_{40} (97.65 m^2/g), but much smaller than amorphous CN (135.76 m^2/g). These results suggest that the introduction of pyrimidine rings would not significantly change the specific surface area, while the increase in crystallinity would reduce the specific surface area.

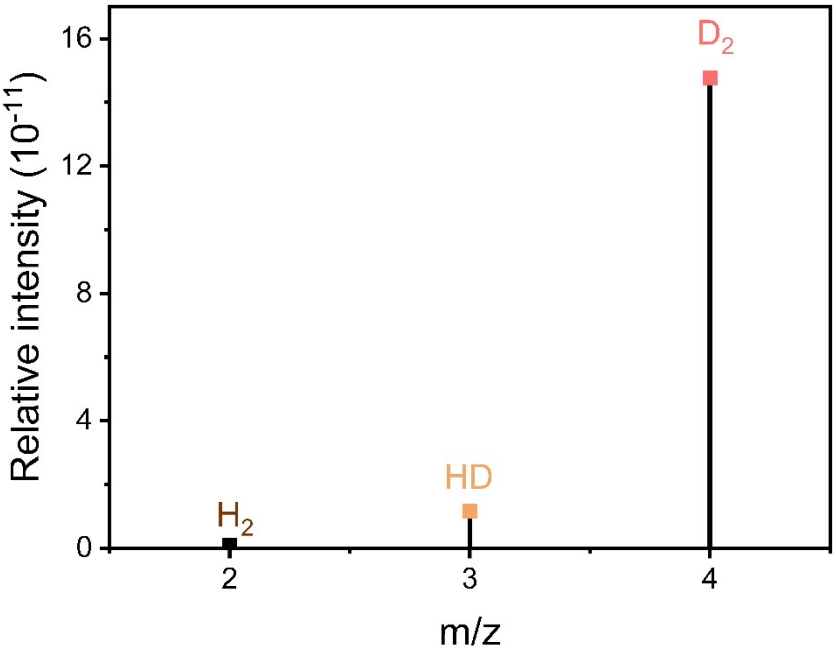

Fig. S6 Mass spectra of the photocatalytically produced hydrogen over CCN-Pr_{40} in deuterium oxide solution (D_2O) containing benzyl alcohol.

The isotopic tracer method was used to clarify the source of evolved H_2, which was carried out in deuterium oxide (D_2O) solution containing benzyl alcohol, and the produced gas (H_2, HD, and D_2) was identified by mass spectrometer (GSD 320, Pfeiffer Vacuum OmniStar). As shown in Fig. S6, the m/z signals at 2, 3, and 4 are indexed to H_2, HD, and D_2, respectively. D_2 (m/z = 4) is detected as the main product with a trace amount of HD (m/z = 3), implying that the hydrogen is mainly evolved via water reduction. The small amount of produced HD could be derived from the dehydrogenation of benzyl alcohol in D_2O solution.[5, 6]

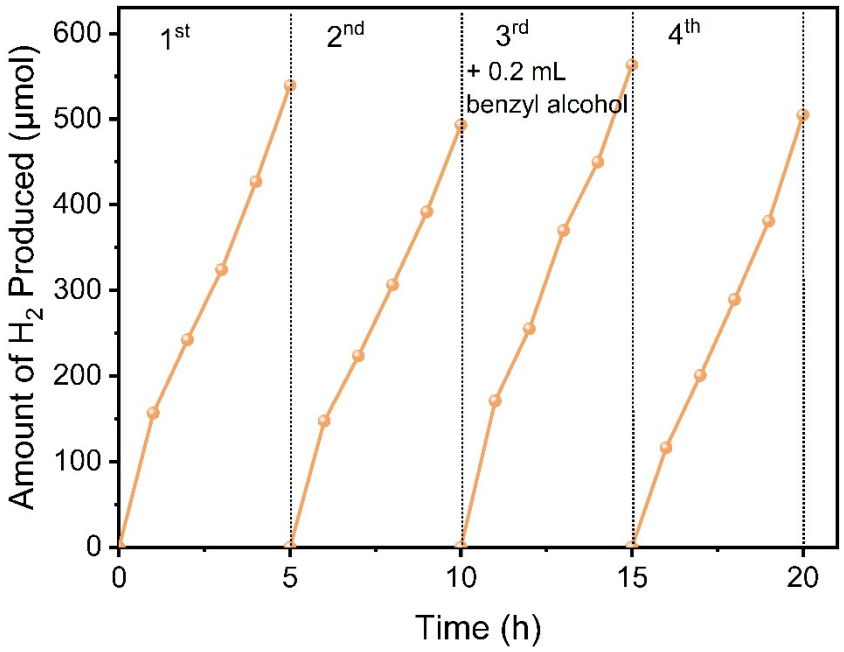

Fig. S7 Stability test of CCN-Pr_{40} for hydrogen evolution in H_2O and benzyl alcohol solution.

With the reaction proceeding, the benzyl alcohol concentration is decreased for the generation of benzaldehyde as oxidation product, which gives rise to the decrease in photocatalytic performance (2nd cycle). With 0.2 mL of benzyl alcohol added in the solution (3rd cycle), the photocatalytic activity is recovered and significantly higher than other cycles, due to the increased benzyl alcohol concentration depending on the addition of benzyl alcohol (0.2 mL).

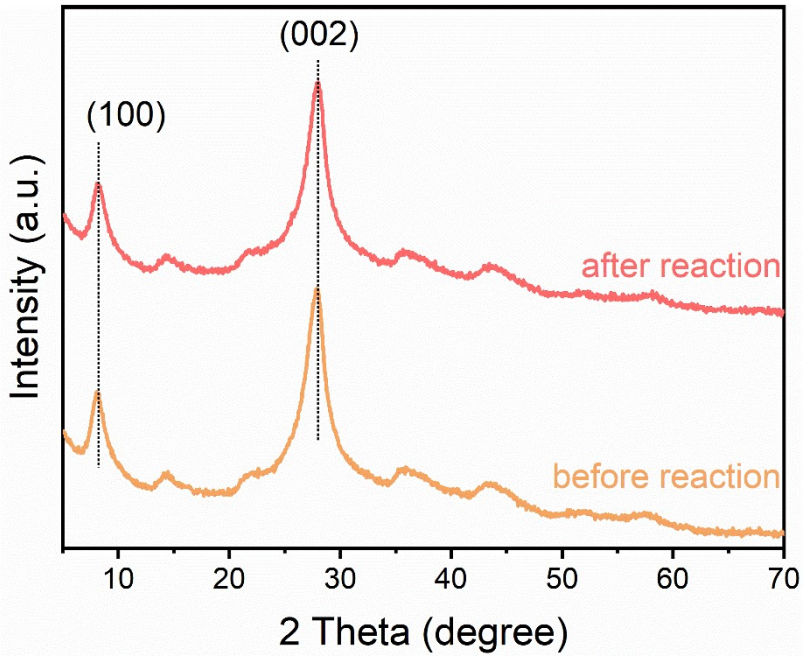

Fig. S8 XRD patterns of CCN-Pr_{40} before and after photocatalytic reaction.

Table S1 Full width at half-maximum (FWHM) values of CN and CCN-Pr_x.

Samples	CN	CCN-Pr_0	CCN-Pr_{20}	CCN-Pr_{40}	CCN-Pr_{60}	CCN-Pr_{80}
FWHM values	3.46	1.91	1.92	1.73	2.15	1.83

Table S2 C, N, and H contents in CCN-Pr_x obtained by elemental analysis.

Samples	Atomic Percentage (%)			Atomic Ratio (C/N)
	C	N	H	
CCN-Pr_0	27.75	43.39	2.39	0.64
CCN-Pr_{20}	28.24	42.94	2.89	0.66
CCN-Pr_{40}	28.48	42.17	2.86	0.68
CCN-Pr_{60}	28.85	41.54	2.81	0.69
CCN-Pr_{80}	29.43	40.74	2.75	0.72

Table S3 Kinetic parameters of charge carrier decay in CN, CCN-Pr_0 and CCN-Pr_{40}.

Samples	τ_1 (ns)	τ_2 (ns)	τ_3 (ns)	τ_{avg} (ns)	χ^2
CN	0.62	3.18	14.18	8.31	1.26
CCN-Pr_0	0.51	2.59	9.78	3.92	1.14
CCN-Pr_{40}	0.48	2.17	9.41	2.19	1.27

Table S4 Summary of PCN-based photocatalysts for photocatalytic hydrogen evolution coupled with selective oxidation of benzyl alcohol to benzaldehyde.

Samples	Reaction conditions	Light source	hydrogen evolution rate ($\mu mol\ h^{-1}$)	benzaldehyde evolution rate ($\mu mol\ h^{-1}$)	Ref.
Co-MoS_2/C_3N_4	20 mg catalyst, 1 vol% BA	LED light (λ = 420 nm)	6.2	9.6	7
CN/BP@Ni	1 mg catalyst, 6 mM BA	LED light (λ = 420 nm)	1.31	/	8
cMel-5	50 mg catalyst, 10 mM BA	Xe lamp (λ > 420 nm)	49.1	44.2	9
SCN-HMS	10 mg catalyst, 1.05 vol% BA	Xe lamp (λ > 420 nm)	3.76	3.87	10
CMCN	20 mg catalyst, 10 mM BA	Xe lamp (λ > 420 nm)	5.76	4.6	11
W_{SA}-CN-PUNS	10 mg catalyst, 1.05 vol% BA	Xe lamp (λ > 420 nm)	2.99	3.05	12
Ru/g-C_3N_{4-x}	5 mg catalyst, 1 vol% BA	Xe lamp (Full spectrum)	32.1	25.35	13
ACN14-1.0%	20 mg catalyst, 40 vol% BA	Xe lamp with AM1.5G filter	95.3	103.9	14
CCN-Pr_{40}	20 mg catalyst, 1.25 vol% BA	Xe lamp with AM1.5G filter	149.39	154.62	This work

BA: benzyl alcohol

Table S5 Benzyl alcohol and benzaldehyde concentrations before and after the 12-h photocatalytic reaction.

Samples	Before reaction (mM)		After reaction (mM)	
	Benzyl alcohol	Benzaldehyde	Benzyl alcohol	Benzaldehyde
CN	7.83	0	5.01	2.52
CCN-Pr_0	7.31	0	1.95	4.71
CCN-Pr_{40}	7.12	0	0.65	6.42

The conversion and selectivity for selective oxidation of benzyl alcohol to benzaldehyde during a 12-hour reaction were implemented in a hermetic Pyrex glass reactor (105 mL), and a 300 W Xe lamp (Microsolar 300, Beijing Perfectlight) equipped with an AM1.5G filter was used as the light source. In a typical reaction, 20 mg of photocatalyst powders were dispersed into an aqueous solution (80 mL) containing benzyl alcohol (60 μL). 2.0 wt% Pt cocatalyst was in-situ loaded on the photocatalyst by photodeposition of H_2PtCl_6. The reactor was purged with argon for 30 min before reaction to remove residual air, and the reaction temperature was controlled at 35 ºC by a cooling water flow. The concentrations of benzyl alcohol and benzaldehyde in solutions were measured by liquid H^1 nuclear magnetic resonance (H^1-NMR).

For CN:

$$\text{Conversion} = \frac{7.83 - 5.01}{7.83} \times 100\% = 36\%$$

$$\text{Selectivity} = \frac{2.52}{7.83 - 5.01} \times 100\% = 89\%$$

For CCN-Pr_0:

$$\text{Conversion} = \frac{7.31 - 1.95}{7.31} \times 100\% = 73\%$$

$$\text{Selectivity} = \frac{4.71}{7.31 - 1.95} \times 100\% = 89\%$$

For CCN-Pr_{40}:

$$\text{Conversion} = \frac{7.12 - 0.65}{7.12} \times 100\% = 91\%$$

$$\text{Selectivity} = \frac{6.42}{7.12 - 0.65} \times 100\% = 99\%$$

Table S6 Calculated STH values of 11 separate CCN-Pr_{40} samples for photocatalytic hydrogen evolution in H_2O and benzyl alcohol solution under one-sun illumination.

No.	H_2 evolved (μmol/2h)	STH(%)
1	50.74	0.74
2	53.36	0.78
3	47.42	0.69
4	50.56	0.74
5	47.65	0.69
6	53.33	0.78
7	50.20	0.73
8	52.34	0.76
9	48.82	0.71
10	50.95	0.75
11	52.05	0.76

Taking NO.1 STH measurement as an example, STH was calculated from Equation (2):

$$\text{STH}(\%) = \frac{\text{Energy of generated hydrogen}}{\text{Solar energy irradiating the reactor}} \times 100\%$$

$$= \frac{n \times \triangle G}{P \times S \times t} \times 100\%$$

$$= \frac{50.74 \times 10^{-6} \times 237130}{100 \times 10^{-3} \times 2.25 \times 2 \times 3600} \times 100\%$$

$$= 0.74\%$$

Table S7 Previously reported PCN-based photocatalysis for hydrogen evolution in sacrificial reagent solutions.

Samples	Sacrificial Reagent	AQY	STH	Ref.
cPCNt-200/1.5	Triethanolamine	13.0% at 420 nm	/	15
C_{ring}-PHCN	Triethanolamine	10.62% at 420 nm	/	16
KCN	Triethanolamine	20.5% at 420 nm	/	17
CMCCN-5	Triethanolamine	26.9% at 420 nm	/	18
$U/AC_{0.5}$	Triethanolamine	13.0% at 420 nm	/	19
Co-CCN/PTI	Triethanolamine	20.88% at 425 nm	/	20
TKCN	Triethanolamine	23.5% at 420 nm	/	21
KCCN	Triethanolamine	25.7% at 420 nm		22
BMCN0.1	Triethanolamine	17.8% at 420 nm	/	23
RPCN	Triethanolamine	21% at 420 nm	/	24
Pt/t-ZrO_2/g-C_3N_4	Triethanolamine	/	0.22%	25
g-C_3N_4/COFs	Triethanolamine	4.07% at 450 nm	0.19%	26
CCN-Pr_{40}	Triethanolamine	27.42% at 420 nm	/	This work
CCN-Pr_{40}	Benzyl Alcohols Oxidation	20.27% at 420 nm	0.74%	This work

Table S8 Elemental contents of CCN-Pr_{40} before and after photocatalytic reaction.

Samples	Atomic Percentage (%)			Atomic Ratio (C/N)
	C	N	H	
Before reaction	28.48	42.17	2.86	0.68
After reaction	28.64	42.07	2.92	0.68

3. References

1. S. J. Clark, M. D. Segall, C. J. Pickard, P. J. Hasnip, M. I. Probert, K. Refson and M. C.Payne, First principles methods using CASTEP, Z. Kristallogr. Cryst. Mater., 2005, 220(5–6), 567-570.
2. K. Gelderman, L. Lee and S. W. Donne, Flat-Band Potential of a Semiconductor: Using the Mott–Schottky Equation, *J. Chem. Edu.*, 2007, **84**, 685.
3. J. Xiao, Y. Xie, F. Nawaz, S. Jin, F. Duan, M. Li and H. Cao, Super synergy between photocatalysis and ozonation using bulk g-C_3N_4 as catalyst: A potential sunlight/O_3/g-C_3N_4 method for efficient water decontamination, *Appl. Catal. B: Environ.*, 2016, **181**, 420-428.
4. S. Chu, Y. Wang, Y. Guo, J. Feng, C. Wang, W. Luo, X. Fan and Z. Zou, Band Structure Engineering of Carbon Nitride: In Search of a Polymer Photocatalyst with High Photooxidation Property, *ACS Catal.*, 2013, **3**, 912-919.
5. J. Luo, M. Wang, L. Chen and J. Shi, Efficient benzaldehyde photosynthesis coupling photocatalytic hydrogen evolution, *J. Energy Chem.*, 2022, **66**, 52-60.
6. X. Xiang, B. Zhu, J. Zhang, C. Jiang, T. Chen, H. Yu, J. Yu and L. Wang, Photocatalytic H_2-production and benzyl-alcohol-oxidation mechanism over CdS using Co^{2+} as hole cocatalyst, *Appl. Catal. B: Environ.*, 2023, **324**, 122301.
7. Y. Hu, X. Yu, Q. Liu, L. Wang and H. Tang, Highly metallic Co-doped MoS_2 nanosheets as an efficient cocatalyst to boost photoredox dual reaction for H_2 production and benzyl alcohol oxidation, *Carbon*, 2022, **188**, 70-80.
8. M. Wen, N. Yang, J. Wang, D. Liu, W. Zhang, S. Bian, H. Huang, X. He, X. Wang, S. Ramakrishna, P. K. Chu, S. Yang and X. F. Yu, Activating Carbon Nitride by BP@Ni for the Enhanced Photocatalytic Hydrogen Evolution and Selective Benzyl Alcohol Oxidation, *ACS Appl. Mater. Interf.*, 2021, **13**, 50988-50995.
9. T. Huo, Q. Deng, F. Yu, G. Wang, Y. Xia, H. Li and W. Hou, Ion-Induced Synthesis of Crystalline Carbon Nitride Ultrathin Nanosheets from Mesoporous Melon for Efficient Photocatalytic Hydrogen Evolution with Synchronous Highly Selective Oxidation of Benzyl Alcohol, *ACS Appl. Mater. Interf.*, 2022, **14**, 13419-13430.
10. F. Zhang, J. Li, H. Wang, Y. Li, Y. Liu, Q. Qian, X. Jin, X. Wang, J. Zhang and G. Zhang, Realizing synergistic effect of electronic modulation and nanostructure engineering over graphitic carbon nitride for highly efficient visible-light H_2 production coupled with benzyl alcohol oxidation, *Appl. Catal. B: Environ.*, 2020, **269**, 118772.
11. H. Wang, J. Zhang, X. Jin, X. Wang, F. Zhang, J. Xue, Y. Li, J. Li and G. Zhang, General surface grafting strategy-derived carbon-modified graphitic carbon nitride with largely enhanced visible light photocatalytic H_2 evolution coupled with benzyl alcohol oxidation, *J. Mater. Chem. A*, 2021, **9**, 7143-7149.
12. F. Zhang, J. Zhang, H. Wang, J. Li, H. Liu, X. Jin, X. Wang and G. Zhang, Single tungsten atom steered band-gap engineering for graphitic carbon nitride

ultrathin nanosheets boosts visible-light photocatalytic H_2 evolution, *Chem. Eng. J.*, 2021, **424**, 130004.
13. Q. Yang, T. Wang, Z. Zheng, B. Xing, C. Li and B. Li, Constructing interfacial active sites in Ru/g-C_3N_{4-x} photocatalyst for boosting H_2 evolution coupled with selective benzyl-alcohol oxidation, *Appl. Catal. B: Environ.*, 2022, **315**, 121575.
14. B. Wu, L. Zhang, B. Jiang, Q. Li, C. Tian, Y. Xie, W. Li and H. Fu, Ultrathin Porous Carbon Nitride Bundles with an Adjustable Energy Band Structure toward Simultaneous Solar Photocatalytic Water Splitting and Selective Phenylcarbinol Oxidation, *Angew. Chem. Int. Ed.*, 2021, **60**, 4815-4822.
15. Z. Liang, X. Zhuang, Z. Tang, Q. Deng, H. Li and W. Kang, High-crystalline polymeric carbon nitride flake composed porous nanotubes with significantly improved photocatalytic water splitting activity: The optimal balance between crystallinity and surface area, *Chem. Eng. J.*, 2022, **432**, 134388.
16. X. Wu, H. Fan, W. Wang, L. Lei, X. Chang and L. Ma, Multiple ordered porous honeycombed g-C_3N_4 with carbon ring in-plane splicing for outstanding photocatalytic H_2 production, *J. Mater. Chem. A*, 2022, **10**, 17817-17826.
17. G. Zhang, Y. Xu, C. He, P. Zhang and H. Mi, Oxygen-doped crystalline carbon nitride with greatly extended visible-light-responsive range for photocatalytic H_2 generation, *Appl. Catal. B: Environ.*, 2021, **283**, 119636.
18. J. Li, X. Liu, H. Che, C. Liu and C. Li, Facile construction of O-doped crystalline/non-crystalline g-C_3N_4 embedded nano-homojunction for efficiently photocatalytic H_2 evolution, *Carbon*, 2021, **172**, 602-612.
19. X. Wang, Y. Zhao, H. Tan, H. Sun, Q. Shang, X. Zhao, T. Qiu and Y. Li, Foamer-Derived Bulk Nitrogen Defects and Oxygen-Doped Porous Carbon Nitride with Greatly Extended Visible-Light Response and Efficient Photocatalytic Activity, *ACS Appl. Mater. Interf.*, 2021, **13**, 23866-23876.
20. S. Shen, J. Chen, Y. Wang, C.-L. Dong, F. Meng, Q. Zhang, Y. Huangfu, Z. Lin, Y.-C. Huang, Y. Li, M. Li and L. Gu, Boosting photocatalytic hydrogen production by creating isotype heterojunctions and single-atom active sites in highly-crystallized carbon nitride, *Sci. Bull.*, 2022, **67**, 520-528.
21. G. Zhang, Y. Xu, H. Mi, P. Zhang, H. Li and Y. Lu, Donor Bandgap Engineering without Sacrificing the Reduction Ability of Photogenerated Electrons in Crystalline Carbon Nitride, *ChemSusChem*, 2021, **14**, 4516-4524.
22. G. Zhang, Y. Xu, D. Yan, C. He, Y. Li, X. Ren, P. Zhang and H. Mi, Construction of K^+ Ion Gradient in Crystalline Carbon Nitride to Accelerate Exciton Dissociation and Charge Separation for Visible Light H_2 Production, *ACS Catal.*, 2021, **11**, 6995-7005.
23. G. Zhang, Y. Xu, G. Liu, Y. Li, C. He, X. Ren, P. Zhang and H. Mi, Pyrimidine donor induced built-in electric field between melon chains in crystalline carbon nitride to facilitate excitons dissociation, *Chin. Chem. Lett.*, 2022, **34**, 107383.
24. Y. Xu, M. Fan, W. Yang, Y. Xiao, L. Zeng, X. Wu, Q. Xu, C. Su and Q. He, Homogeneous Carbon/Potassium-Incorporation Strategy for Synthesizing Red

Polymeric Carbon Nitride Capable of Near-Infrared Photocatalytic H_2 Production, *Adv. Mater.*, 2021, **33**, 2101455.

25. H. Li, Y. Wu, C. Li, Y. Gong, L. Niu, X. Liu, Q. Jiang, C. Sun and S. Xu, Design of Pt/t-ZrO_2/g-C_3N_4 efficient photocatalyst for the hydrogen evolution reaction, *Appl. Catal. B: Environ.*, 2019, **251**, 305-312.
26. L. Wang, R. Lian, Y. Zhang, X. Ma, J. Huang, H. She, C. Liu and Q. Wang, Rational preparation of cocoon-like g-C_3N_4/COF hybrids: Accelerated intramolecular charge delivery for photocatalytic hydrogen evolution, *Appl. Catal. B: Environ.*, 2022, **315**, 121568.